ELSEVIER

Contents lists available at ScienceDirect

Journal of Membrane Science

journal homepage: www.elsevier.com/locate/memsci



Full length article

Generating buoyancy-driven convection in membrane distillation

Miles Mabry ^a, Federico Municchi ^a, Yiming Liu ^b, Jingbo Wang ^b, Tzahi Y. Cath ^c, Craig S. Turchi ^d, Michael B. Heeley ^e, Eric M.V. Hoek ^{b,f}, David Jassby ^b, Denis Martinand ^g, Nils Tilton ^{a,*}

- a Colorado School of Mines, Department of Mechanical Engineering, Golden, CO, USA
- b University of California Los Angeles (UCLA), Department of Civil & Environmental Engineering, California NanoSystems Institute and Institute of the Environment & Sustainability, Los Angeles, CA, USA
- ^c Colorado School of Mines, Department of Civil & Environmental Engineering, Golden, CO, USA
- ^d Buildings & Thermal Science Center, National Renewable Energy Laboratory, Golden, CO, USA
- e Center for Entrepreneurship, College of Engineering, University of Michigan, Ann Arbor, MI, USA
- ^f Energy Storage & Distributed Resources Division, Lawrence Berkeley National Lab, Berkeley, CA, USA
- g CNRS, Centrale Marseille, M2P2, Aix-Marseille University, Marseille, France

ARTICLE INFO

Keywords: Membrane distillation Buoyancy-driven convection Temperature polarization Concentration polarization

ABSTRACT

Membrane distillation (MD) is a thermally-driven desalination process that can treat hypersaline brines. Considerable MD literature has focused on mitigating temperature and concentration polarization. This literature largely neglects that temperature and concentration polarization increase the feed density near the membrane. With gravity properly oriented, this increase in density could trigger buoyancy-driven convection and increase permeate production. Convection could also be strengthened by heating the feed channel wall opposite the membrane. To investigate that possibility, we perform a series of experiments using a plate-and-frame direct contact MD system with an active membrane area of 300 cm² and a feed channel wall heated using a resistive heater. The experiments measure the average transmembrane permeate flux for two gravitational orientations, feed Reynolds numbers between 128 and 1128, and wall heat fluxes up to $12 \, \text{kW/m}^2$. The results confirm that with gravity properly oriented, wall-heating can trigger buoyancy-driven convection for a wide range of feed Reynolds numbers, and increase permeate production between roughly 20 and 130 %. We estimate, however, that at high Reynolds numbers (Re > 800), more than 70 % of the wall heat is carried out of the MD system by the feed flow, without contributing to permeate production. This suggests the need for longer membranes and heat recovery steps in any future practical implementation.

1. Introduction

Membrane distillation (MD) is a thermally driven desalination process that has been studied extensively in prior literature because it can treat hypersaline brines [1,2]. MD operates by flowing warm feed over a hydrophobic microporous membrane, as in Fig. 1(a). A difference in partial vapor pressure across the membrane causes water to evaporate at the feed surface of the membrane and diffuse through the membrane as vapor. Nonvolatile solutes remain in the feed. Depending on the approach to MD, the vapor condenses either in the permeate channel or in a separate condenser. In the simplest approach, called direct contact membrane distillation (DCMD), the vapor condenses in a stream of cool distillate water flowing over the permeate surface of the membrane. This method is arguably the most popular approach to MD, but suffers from conductive heat losses through the membrane [3]. Alternate

approaches reduce these losses by maintaining a layer of air over the permeate surface of the membrane, as in air gap membrane distillation (AGMD), or by drawing the permeate vapor out of the permeate channel and into a separate condenser, as in vacuum membrane distillation (VMD) and sweep gas membrane distillation (SGMD). The drawback to these approaches is a sharp increase in system complexity.

The primary attraction of MD is that it is less sensitive to osmotic pressure than reverse osmosis (RO). While conventional RO can treat NaCl solutions to between 70–100 g/L, MD treatments are reported near 300 g/L [4,5]. A secondary attraction is that MD operates at feed temperatures below 90 °C. These can be produced by solar energy and low-grade heat from industrial or geothermal sources to reduce energy consumption. Nevertheless, MD faces two long-standing challenges. The first, called *temperature polarization*, is the cooling of feed in a

E-mail address: ntilton@mines.edu (N. Tilton).

^{*} Corresponding author.

Nomenclature	
Abbreviations	
AGMD	Air gap membrane distillation.
CFD	Computational fluid dynamics.
DCMD	Direct contact membrane distillation.
LMH	Liters per square meter per hour (l/(m ² h)).
MD	Membrane distillation.
SGMD	Sweep gas membrane distillation.
VMD	Vacuum membrane distillation.
Symbols	
α	Linear rate of increase of J with q
	(LMH/W). See Fig. 7.
β^{cnd}	Percentage of q_p lost to transmembrane
	heat conduction (unitless). See Eq. (3).
β^{evp}	Percentage of q_p lost to evaporation (unitless). See Eq. (3).
β^{loss}	Percentage of q_p lost to the environment (unitless). See Eq. (3).
β^{out}	Percentage of q_p exiting the feed outlet (unitless). See Eq. (4).
ΔJ	Relative percent increase in J between $q_p =$
49	0 and $q_p = 360$ W (unitless). See Table 1.
\dot{m}_{in}^d	Distillate inlet mass flow rate (kg/s). See
in	Fig. 5.
\dot{m}_{out}^d	Distillate outlet mass flow rate (kg/s). See Fig. 5.
\dot{m}_{in}^f	Feed inlet mass flow rate (kg/s). See Fig. 5.
min m ^f _{out}	Feed outlet mass flow rate (kg/s). See Fig. 5.
η_p	The fraction $\beta^{evp}/(\beta^{evp}+\beta^{end})$ (unitless). See Eq. (6).
v^d	Inlet distillate kinematic viscosity (m^2/s).
in f	Inlet feed kinematic viscosity (m²/s).
v_{in}^d v_{in}^f c_p^d	Specific heat evaluated at the distillate inlet
	(J/(kg K)). See Fig. 5.
c_p^f	Specific heat evaluated at the feed inlet
	(J/(kg K)). See Fig. 5.
D_h	Hydraulic diameter (m)
g	Gravitational acceleration (m/s²).
h	Feed and distillate channel height, set to $h = 2$ mm throughout.
J	Average transmembrane permeate flux (LMH).
J_0	Average transmembrane permeate flux when $q_p = 0$ (LMH).
J_{360}	Average transmembrane permeate flux when $q_p = 360$ W (LMH).
q_{cnd}^0	q_{evp} when $q_p = 0$ (W). See Eq. (3).
q_{evp}^0	q_{evp} when $q_p = 0$ (W). See Eq. (3).
q_{evp}^0 q_{loss}^0	q_{evp} when $q_p = 0$ (W). See Eq. (3). q_{loss} when $q_p = 0$ (W). See Eq. (3).
q_{loss} q_p	Power provided by heated plate (W). See
q_{cnd}	Fig. 5. Energy lost to transmembrane heat conduc-
-cnu	tion (W). See Fig. 5.

thermal boundary layer growing along the membrane. This reduces vapor production as feed flows downstream. The second challenge, called *concentration polarization*, is the accumulation of solutes near the

$q_{e_{UD}}$	Energy lost to evaporation (W). See Fig. 5.			
q_{loss}	Energy lost to the environment (W). See			
11033	Fig. 5.			
$Re^d = U_{in}^d D_h / v_{in}^d$	Inlet distillate Reynolds number (unitless).			
$Re^f = U_{in}^f D_h / v_{in}^f$	Inlet feed Reynolds number (unitless).			
SD	Standard deviation. See Eq. (5).			
T_{in}^d	Distillate inlet temperature (°C). See Fig. 5.			
T_{out}^d	Distillate outlet temperature (°C). See			
_	Fig. 5.			
T_{in}^f	Feed inlet temperature (°C). See Fig. 5.			
$T_{in}^f \ T_{out}^f \ T^{f,0}$	Feed outlet temperature (°C). See Fig. 5.			
$T_{out}^{f,0}$	Feed outlet temperature when $q_p = 0$ (°C).			
	See Eq. (4).			
U^d_{in}	Mean inlet distillate velocity (m/s).			
U_{in}^f	Mean inlet feed velocity (m/s).			

membrane. Though this decreases the feed partial vapor pressure, the effect is often considered mild compared to temperature polarization. The greater risk is that concentration polarization leads to *mineral scaling*, which is the precipitation of salts onto the membrane, where they can block or flood pores.

1.1. Motivation

The current work is motivated by recent studies that mitigate temperature polarization using composite membranes heated by resistive heating [6-9], induction heating [10], solar irradiation [11,12], or lateral thermal conduction [13-15]. Though promising, heated membranes present some challenges. (1) When used in DCMD, heated membranes lose heat to the cool permeate flow, and exacerbate temperature polarization in the permeate channel. Consequently, heated membranes are primarily proposed for VMD, AGMD, and SGMD, which are significantly more complicated [6,7,10,13,15]. (2) Membranes heated by solar irradiation must be spread over a large area, in direct contact with sunlight [11,12]. There are also open questions about the long term impact of solar radiation on polymers used in many membrane materials. Studies consequently focus on heating membranes electrically, which increases the energy demand. (3) Heated membranes perform best at low feed flow rates that maximize contact time with the feed [10]. Studies of heated membranes in bench-scale plate-and-frame systems consider feed Reynolds numbers as low as Re = 0.1, where Re is based on the mean feed velocity and feed channel hydraulic diameter [8]. Though such low Reynolds numbers improve heat transport to the feed, they can also increase concentration polarization and mineral scaling [15], which are major concerns when treating hypersaline brines. For that reason, MD systems with plate-and-frame or spiral wound geometries are typically operated at Reynolds numbers in the range $100 \le Re \le 1000$ [16,17]. Though not considered in the current study, hollow fiber MD modules are also typically operated at large cross flow velocities to mitigate polarization.

The current work is further motivated by the fact that little prior work has considered that temperature and concentration polarization cause an increase in the feed density near the membrane [18–21]. In a recent computational fluid dynamics (CFD) study [22], we show that with gravity pointing towards the feed channel wall, as in Fig. 1(b), the local increase in density can trigger a buoyancy-driven instability, in which plumes of dense solute-rich feed sink away from the membrane. The sinking plumes bring warm low-concentration feed to the membrane, and increase permeate production. Our CFD [22] also shows that in this unstable orientation, buoyancy-driven convection can be strengthened and sustained over long membranes (at Reynolds numbers above Re > 100) by actively heating the channel wall opposite the

Fig. 1. (a) Sketch (not to scale) of an MD system in a stable-orientation for which gravity points away from the feed channel wall. The membrane is shaded gray. The dotted region shows the concentration boundary layer. The temperature profile illustrates temperature polarization. (b) Sketch of an MD system in an unstable-orientation for which gravity points towards the feed channel wall.

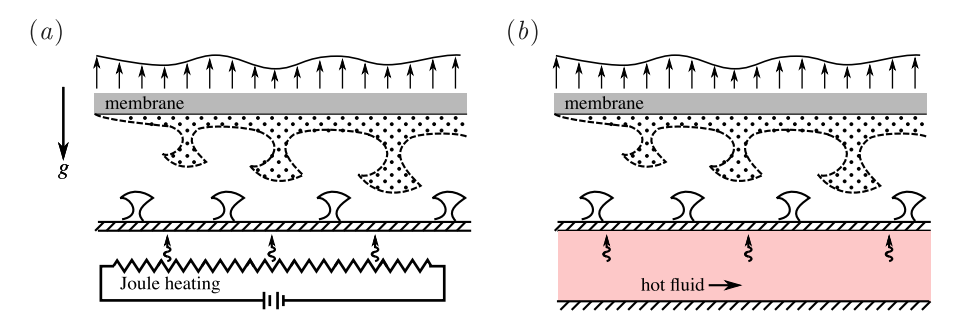


Fig. 2. Convection can be strengthened and sustained over long membranes by heating the feed channel wall using resistive Joule heating (panel a) or a secondary hot fluid (panel b).

membrane. This generates rising plumes of warm fluid that reinforce instability and replenish heat lost to evaporation at the membrane surface, as in Fig. 2. The plate can be heated using resistive Joule heating, as sketched in Fig. 2(a), or by flowing a secondary hot fluid over the opposite surface of the plate, as in Fig. 2(b). That secondary fluid can in turn be heated by solar, geothermal, or industrial low-grade heat. In this manner, buoyancy-driven convection could mitigate temperature polarization without requiring novel membrane development or additional electric heating.

1.2. Objectives

Thus motivated, the objective of the current study is to experimentally confirm whether wall heating can trigger buoyancy-driven convection in DCMD, and if so, for what operating conditions. We believe that fundamental question deserves to be answered before pursuing any practical implementation of wall-heating in MD. If warranted, that latter exploration is left to future work. We also note that confirmation of buoyancy-driven convection in the current study would suggest that buoyancy should be explored for heated membranes as well, particularly as those studies tend to focus on low Reynolds numbers for which turbulent mixing is not possible.

To supply wall-heating, we develop a bench-scale, plate-and-frame, DCMD system in which the feed channel has a smooth stainless steel plate heated with a thin resistive heater (detailed in Section 2). The heated plate and active membrane both have a width and length of 10 cm and 30 cm, respectively. The active membrane area (300 cm²) is much larger than those typically considered bench-scale systems, which tend to consider areas between 0.25 to 30 cm² [6-8,10,11,13]. Using our system, we perform a parametric study in which we systematically measure the average transmembrane permeate flux for a range of wall heat flux and feed Reynolds number. The latter varies between 128 ≤ $Re \leq 1148$, which covers the range typically considered in plate-andframe and spiral wound membrane modules [17]. It is worth stressing that MD literature typically suggests the process should be operated at large Reynolds numbers. However, those works are not necessarily relevant here, because they focus on "conventional" MD, in which the feed is only heated before entering the membrane module. We also

note that choosing an optimal Reynolds number depends on how it influences both permeate production and mineral scaling. Because the current study does not consider mineral scaling, we make no claims as to what an optimal operating Reynolds number might be.

We perform our experiments with the membrane oriented horizontally, and the experiments are repeated for the two gravitational orientations shown in Fig. 1. In the stable orientation sketched in panel (a), the feed flows above the membrane, such that gravity points towards the membrane feed surface. In the unstable orientation sketched in panel (b), the feed flows below the membrane, such that gravity points away from the membrane feed surface. All experiments are performed in triplicate, using fresh membrane coupons. We also perform an energy balance to estimate the fraction of wall heating that successfully contributes to permeate production. Most experiments use a feed solution of DI water and 70 g/L NaCl, which is typical of waste brine produced by RO. Most experiments are performed without a feed spacer, because our long term goal is to texture the heated surface with fins or dimples (see Fig. 13) that support the membrane while promoting heat transport or mitigating concentration polarization [17].

Note that our previous CFD study [22] simulated buoyancy-driven convection in VMD, which is simpler to simulate because the flow in the permeate channel can be neglected. However, our experience is that VMD is more difficult to implement experimentally due to the challenges of (1) sealing and maintaining a low vacuum pressure in the permeate channel, (2) preventing vapor condensation within the permeate channel, and (3) accurately measuring the condensation rate in the condenser. These challenges reduce the accuracy and repeatability of the measured rate of permeate production. Because we rely on that data as evidence of buoyancy-driven convection, we use a DCMD system for which we have an established record of measuring accurate data [5,16,23,24]. We also stress here that comparison with CFD simulations of our current system is outside the reasonable scope of the current study, because buoyancy-driven convection in MD is uniquely challenging to simulate accurately [22]. One major challenge arises because wall heating generates variations in feed viscosity and mass diffusivity on the order of 100%, and variations in feed density on the order of 10%. The latter pushes the limits of the Boussinesq approximation, such that accurate CFD requires a low-Mach-number

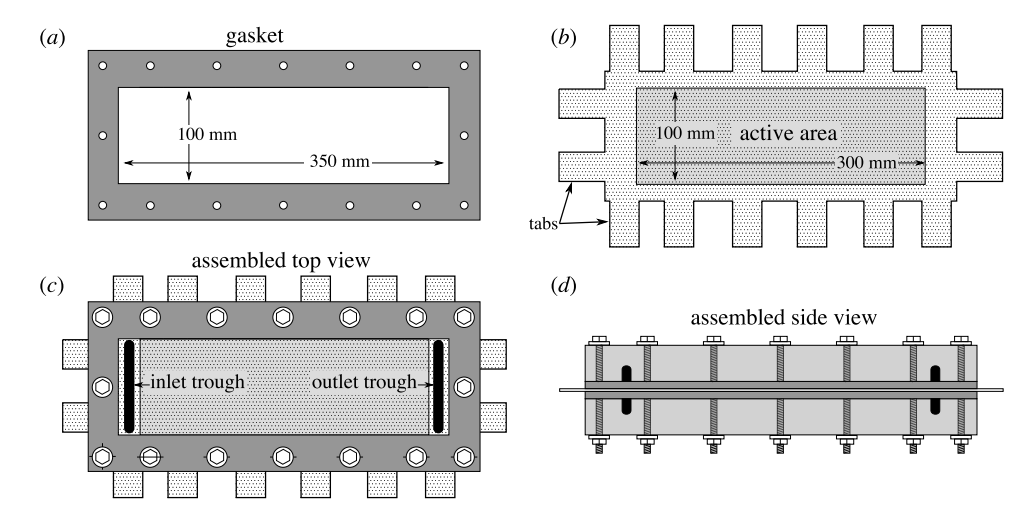


Fig. 3. Sketch (not to scale) demonstrating how the feed and distillate channels are sealed using two acrylic plates, two gaskets, and a membrane sheet. Panel (a) shows a gasket. Panel (b) shows a membrane with tabs. Panels (c) and (d) show assembled top and side views, with the inlet and outlet troughs shaded black. These troughs are further illustrated in Fig. 4. In all panels, the membrane is oriented horizontally, and the feed and distillate flow from left to right.

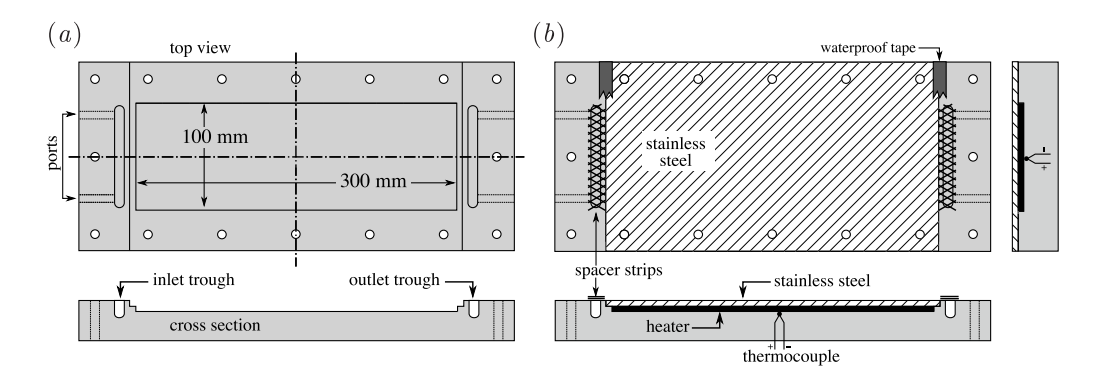


Fig. 4. Sketch (not to scale) of the heated plate. Panel (a) shows the milled acrylic plate. Panel (b) shows the assembled plate with the resistive heater, steel plate, and thermocouple. In both panels, the heated surface is oriented horizontally, and feed and distillate flow from left to right.

variable-density solver. These are computationally expensive (in terms of CPU hours) for the conditions experienced in MD [22,25]. Our CFD work also shows that simulations require fine grids and time steps to resolve small flow structures in the boundary layers and plumes [22]. These compounding issues make the 3D simulation of our large bench-scale system unfeasible for the current scope.

The remaining study is organized as follows. Section 2 presents our experimental methods, data processing, and an energy balance. Section 3 interprets the results of a parametric study. Section 4 summarizes our conclusions.

2. Methods

The objective of our experiments is to measure the average transmembrane permeate flux J in a plate-and-frame DCMD system with a heated feed channel wall. We repeat measurements for the stable and unstable orientations labeled in Fig. 1, and we attribute the impact on J to buoyancy-driven convection. We also perform an energy balance to estimate the percentage of wall heat that contributes to permeate production.

2.1. Flow cell

Our experiments use the DCMD cell illustrated in Fig. 3, which was the result of considerable trial and error detailed in Ref. [26]. It was chosen because it produces highly repeatable data, and can be easily extended to longer channel widths and lengths. The feed and distillate channels are formed by cutting the desired channel width and length

(100 mm \times 350 mm) from two identical 2.3 mm thick rubber gaskets (panel a). The gaskets are placed on the opposite sides of a membrane (panel b) that has a 100 \times 300 mm² active area and tabs extending beyond the gaskets. Outside the active area, the membrane surface is sealed with silicone. The gaskets and membrane are sealed between two acrylic plates using bolts (panels c and d). As the bolts are tightened, we pull the tabs to remove wrinkles from the membrane. Feed and distillate enter and exit the flow channels through troughs that distribute flow across the channel width. The troughs (shown in black in panels c and d) are outside the active membrane area. Each trough is connected to two ports drilled through the acrylic plate, as shown in Fig. 4.

Note that our active membrane area (300 cm²) is much larger than that typically considered in past literature [6-8,10,11,13], which considers areas between roughly 0.25 to 30 cm². Though our design can be easily increased to larger membrane areas, that becomes prohibitively expensive in the current study, due to the large amount of membrane material required to perform all experiments in triplicate. To support the membrane, we place a spacer over the full width and length of the permeate channel. The spacer has a height of 2 mm and is made of a non-woven mesh of extruded polypropylene filaments in a diamond pattern. For most experiments, there is no feed spacer over the active area of the membrane. However, there are two small strips of spacer material over the troughs, as sketched in Fig. 4(b). These strips are glued to the acrylic feed plate, outside the active membrane area. The strips ensure the feed and distillate channels have equal heights of h = 2 mm once the bolts are tightened. To minimize membrane flapping, all experiments are performed with the feed and distillate flowing in a cocurrent configuration. The feed inlet pressure is also kept

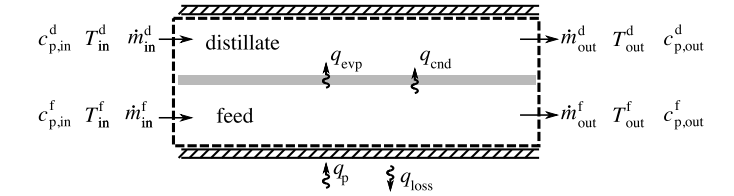


Fig. 5. Control volume used in energy balance.

slightly higher than the inlet distillate pressure to press the membrane against the permeate spacer. Though conventional DCMD systems are often operated in counter-flow mode to minimize temperature polarization, the above measures are taken here to confidently attribute any impact of varying the feed flow rate to buoyancy-driven convection, and not membrane flapping. These measures are also consistent with established practices taken in prior literature when comparing CFD and experiments [16].

All experiments use a Clarcor QP952 membrane with a porosity between 0.70–0.85, and a nominal pore size of 0.45 μ m. The membrane has an active layer of elongated polytetrafluoroethylene (ePTFE) above a non-woven polyester support layer [27]. This membrane is chosen because its support layer reduces membrane warping and increases repeatability. Our prior work also finds that this membrane provides a salt rejection above 99.8% [27].

2.2. Heated plate

We heat the feed channel wall using a thin (1 mm thick) surface heater with a 100 mm width and 300 mm length (Omega Engineering, SRFGA). The heater is placed in a cavity in the acrylic plate, and covered with a 1.5 mm thick 316 stainless steel plate, as in Fig. 4. The steel plate sits in a recess milled in the acrylic to provide a flush surface in the feed channel. The steel is sealed to the acrylic using silicone sealant (General Electric Sealants). The contact lines between the steel and acrylic are also sealed with Nashua waterproofing foil tape, as in Fig. 4(b). Once assembled, the 100 mm \times 300 mm heater surface is situated opposite from the 100 mm \times 300 mm active membrane area.

Several thin sheets of silicone are placed between the heater and acrylic plate to press the heater firmly against the steel plate. A k-type thermocouple is placed in the silicone sheets to monitor the internal temperature of the acrylic plate. To prevent thermal deformation of the acrylic plate, experiments are stopped if the measured temperature exceeds 100 °C. The heater supplies up to 1.55 W per cm² of the heater's 300 cm² surface, and is powered by a 500 W adjustable AC power supply (YaeCCC TDGC-0.5KM) run through a ground-fault circuit interrupter in case of an electrical short.

2.3. Energy balance

Only a fraction of the supplied wall heat q_p successfully contributes to feed evaporation. The remaining q_p is lost to transmembrane heat conduction, the surrounding environment, or exits with the feed outlet flow. We estimate these fractions using the control volume shown in Fig. 5. The volume receives energy from the heated plate and channel inlets, while losing energy through the channel outlets and the surrounding environment. A steady-state energy balance produces the following approximation for the environmental loss, labeled q_{loss} ,

$$q_{loss} = q_p + \left[\dot{m} \, c_p \, T \right]_{in}^f + \left[\dot{m} \, c_p \, T \right]_{in}^d - \left[\dot{m} \, c_p \, T \right]_{out}^f - \left[\dot{m} \, c_p \, T \right]_{out}^d, \tag{1}$$

where \dot{m} and c_p denote the feed/distillate mass flow rates and specific heats, respectively. The superscripts f and d refer to quantities evaluated in the feed and distillate, respectively. The subscripts in and out refer to quantities evaluated at the inlets and outlets, respectively, as labeled in Fig. 5. We evaluate \dot{m} using the feed/distillate densities

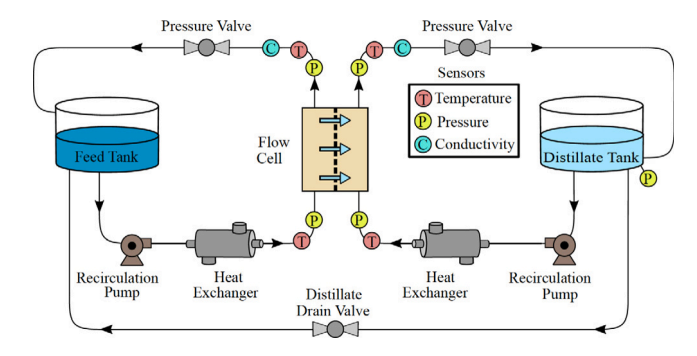


Fig. 6. Flow control and instrumentation of bench scale DCMD system. The feed and distillate loops are depicted on the left and right, respectively side of the figure.

and volumetric flow rates. Densities and specific heats are evaluated at the corresponding inlet/outlet temperature and NaCl concentration, as detailed in Appendix B.

MD literature [1,24] typically approximates the transmembrane heat flux as the sum of a latent heat transfer and conductive heat transfer, labeled q_{evp} and q_{cnd} , respectively, in Fig. 5. We follow prior literature and estimate the latent heat transfer as $q_{evp} = \dot{m}_j \lambda$, where \dot{m}_j is the transmembrane vapor mass flux and λ (J/kg) is the latent heat of evaporation. The latent heat is approximated [24] as $\lambda = 2502800 - 2438.18\,T$, where T is measured in Celsius. We follow the common practice of setting $T = (T_{in}^f + T_{in}^d)/2$. To estimate q_{cnd} , we perform an energy balance for the permeate channel, which produces

$$q_{cnd} = \left[\dot{m} \, c_p \, T \right]_{out}^d - \left[\dot{m} \, c_p \, T \right]_{in}^d - q_{evp}. \tag{2}$$

Eq. (2) assumes that environmental losses primarily occur in the feed channel, because the distillate temperatures are much closer to the ambient lab temperature of roughly $25~^{\circ}$ C.

To determine the fractions of q_p lost to evaporation, transmembrane heat conduction, and the environment, we first compute q_{evp} , q_{cnd} , and q_{loss} by performing an experiment with no wall heat $(q_p=0)$. We then repeat the experiment with nonzero q_p , and estimate the fractions as

$$\beta^{evp} = \frac{q_{evp} - q_{evp}^0}{q_p}, \quad \beta^{cnd} = \frac{q_{cnd} - q_{cnd}^0}{q_p}, \quad \beta^{loss} = \frac{q_{loss} - q_{loss}^0}{q_p}, \quad (3)$$

where the superscript 0 denotes quantities computed at $q_p=0$. To estimate the fraction of q_p exiting the feed outlet, we use the experimentally measured feed outlet temperatures,

$$\beta^{out} = \frac{\left[\dot{m} \, c_p \, T \right]_{out}^f - \left[\dot{m} \, c_p \, T \right]_{out}^{f,0}}{q_p},\tag{4}$$

where the superscript "f,0" denotes results when $q_p = 0$.

2.4. Flow control and instrumentation

The DCMD cell operates in the closed-loop system sketched in Fig. 6. Feed exits a 10 L tank and passes through a pump, digital flow meter, and heat exchanger (Brazetek BT-STX-85) to set the desired feed inlet temperature and volumetric flow rate. The feed then flows through the DCMD cell and returns to the feed tank through the top. This drops returning feed into the tank to enhance mixing. Distilled water similarly exits a 10 L tank and passes through a pump, digital flow meter, heat exchanger (Brazetek BT-STX-85), and the cell. The feed and distillate loops use identical centrifugal pumps (Micropump CA series powered by an EagleDrive DEMSE motor). Distillate returns to the distillate tank through the lower side wall to minimally disturb the water within. This reduces noise measured by a pressure transducer (OMEGA PX309-002GV) placed at the tank base to compute the distillate volume. The distillate tank is placed above the feed tank, and the base of the

Table 1 For the stable (stab.) and unstable (unst.) orientations and feed Reynolds numbers listed in columns 1 and 2, respectively, the remaining columns report U_m^f , J_0 , J_{360} , ΔJ , β^{evp} , β^{end} , β^{out} , and η_q . The β and η_q values are computed when $q_p=240$ W. The data in parentheses represent one standard deviation (SD). To aid readability, the data for the unstable orientation is shaded gray. Note that we set η_p to unity in the stable orientation when $Re^f=893$, due to the unphysical $\beta^{end}=-0.09$ value.

	Re^f	U_{in}^f	J_0	J_{360}	ΔJ	β^{evp}	β^{out}	β^{cnd}	η_q
Units		cm/s	LMH	LMH	%	%	%	%	%
stab.	128	1.64	2.12	3.88	85.1	11.2	61.8	18.4	37.8
			(SD: 0.16)	(SD: 0.63)	(SD: 37)	(SD: 2.9)	(SD: 0.52)	(SD: 0.38)	
unst.	128		3.19	7.56	137	24.8	27.5	35.0	41.5
unot.	120		(SD: 0.029)	(SD: 0.19)	(SD: 6.9)	(SD: 2.3)	(SD: 3.0)	(SD: 0.43)	11.0
stab.	255	3.28	3.42	4.23	23.6	5.29	79.1	7.71	40.7
stab.	200	3.20	(SD: 0.11)	(SD: 0.23)	(SD: 7.2)	(SD: 0.56)		(SD: 1.1)	40.7
unst.	255		5.59	8.66	55.4	19.7	50.0	21.5	47.8
			(SD: 0.41)	(SD: 0.25)	(SD: 6.9)	(SD: 3.6)	(SD: 0.60)	(SD: 2.0)	
stab.	383	4.92	4.31	5.10	18.5	4.72	82.7	2.53	65.1
			(SD: 0.097)	(SD: 0.11)	(SD: 5.1)	(SD: 0.99)	(SD: 1.8)	(SD: 0.76)	
unst.			6.58	9.33	41.9	17.0	56.1	16.8	50.3
			(SD: 0.18)	(SD: 0.14)	(SD: 3.1)	(SD: 2.1)	(SD: 0.68)	(SD: 1.7)	
stab.	510	6.56	5.48	5.76	5.20	1.36	87.4	5.33	20.3
			(SD: 0.30)	(SD: 0.071)	(SD: 4.4)	(SD: 3.0)	(SD: 2.1)	(SD: 1.1)	
unst.	510		6.95	9.48	36.4	15.7	60.3	14.6	51.8
	010		(SD: 0.25)	(SD: 0.52)	(SD: 3.0)	(SD: 1.8)	(SD: 3.6)	(SD: 2.0)	01.0
stab.	638	8.20	5.99	6.48	8.42	2.51	88.6	3.06	45.1
otab.	000	0.20	(SD: 0.30)	(SD: 0.25)	(SD: 5.7)	(SD: 2.5)	(SD: 1.6)	(SD: 1.1)	1011
unst.	638		8.13	10.1	24.5	13.6	69.6	11.1	55.1
			(SD: 0.27)	(SD: 0.22)	(SD: 1.9)	(SD: 1.7)	(SD: 2.5)	(SD: 2.0)	
stab.	893	11.5	6.85	7.71	12.8	4.88	90.8	-0.09	1
			(SD: 0.34)	(SD: 0.19)	(SD: 4.6)	(SD: 2.8)	(SD: 3.2)	(SD: 1.5)	
unst.	893		8.78	10.6	20.4	10.5	77.7	9.83	51.7
			(SD: 0.20)	(SD: 0.18)	(SD: 0.75)	(SD: 1.3)	(SD: 0.76)	(SD: 2.0)	

distillate tank has a solenoid valve that allows a desired volume of distillate to return to the feed tank.

Temperature probes (Electronic Innovations EI1034) and pressure transducers (OMEGA PX309-030G5V) monitor the feed and distillate temperatures and pressures entering and exiting the cell. Probes measure the electrical conductivity of the feed (Sensorex TCSMA Blind Toroidal Conductivity Transmitter) and distillate (Eutech alpha-COND500). Data collection and operating conditions are automated using LabVIEW and a multichannel DAQ. Components of the distillate and feed loop are connected by vinyl tubing insulated with foam, and both tanks are sealed to minimize evaporation.

We compute the average permeate flux J by tracking the water volume in the distillate tank as a function of time. A linear fit is applied to this data, as demonstrated in Appendix A, and the resulting slope is divided by the membrane active area (300 cm²) to obtain J. We report J in units of $L/(m^2 h)$, abbreviated as LMH.

When shutting down the system between experiments, we flush the system with DI water until the feed conductivity probe reads zero conductivity for one hour. When replacing the membrane, we clean the DCMD cell with DI water and dish soap. We also clean the flow control system by flushing for one hour with DI water, followed by one hour with an NaOH solution (pH > 11.5), and one hour of an HCl solution (pH < 2.5). We then flush the system with DI water again until the conductivity probe reads zero for one hour.

2.5. Experimental procedures

Most experiments use a feed solution of DI water and 70 g/L NaCl, which is a common NaCl concentration in waste brine produced by reverse osmosis. To avoid interfering with buoyancy-driven convection, most experiments have no feed spacer over the active membrane area, as sketched in Fig. 4(b). All experiments maintain constant inlet feed

and distillate temperatures of $T_{in}^f=60\pm3$ °C and $T_{in}^d=30\pm1$ °C, respectively. To minimize temperature polarization in the distillate channel, we set the distillate inlet flowrate to the maximum value reliably maintained by our system. This produces a mean distillate inlet velocity of $U_{in}^d=14.8$ cm/s, when averaged over the cross-sectional channel area. That corresponds to an inlet distillate Reynolds number of $Re^d=735$, where $Re^d=U_{in}^dD_h/v_{in}^d$ is defined using the channel hydraulic diameter D_h and the inlet distillate kinematic viscosity v_{in}^d . Most experiments vary the average feed inlet velocity between $1.64 \le U_{in}^f \le 11.5$ cm/s. This varies the inlet feed Reynolds number between $1.28 \le Re^f \le 893$, where $Re=U_{in}^fD_h/v_{in}^f$. A small set of experiments shown in Fig. 9(b) consider the higher Reynolds number $Re_f=1148$. The viscosities v_{in}^d and v_{in}^f are computed using relationships detailed in Appendix B.

A typical series of experiments begins by running the system for an hour without wall-heating ($q_p=0$) to allow the system to reach steady state. We then run the system for one hour each with $q_p=0$, 120, 240, and 360 W. The measured permeate fluxes at these heating levels are denoted J_0 , J_{120} , J_{240} , and J_{360} , respectively. In some cases, we do not consider $q_p=360$ W, because the temperature of the acrylic feed plate, measured by the thermocouple, exceeds 100 °C. We repeat the above procedure for the stable and unstable orientations shown in Fig. 1, and a range of feed Reynolds numbers, Re^f .

All experiments are run in triplicate using fresh membrane coupons to measure repeatability. We compute the standard deviation (SD) of the measured flux using the definition

$$SD = \sqrt{\frac{1}{3} \sum_{i=1}^{3} \left(J_i - \overline{J} \right)} \quad , \tag{5}$$

where J_i is the measured flux from run i, and \overline{J} is the average of three runs. In plots with errors bars, the total error bar length is two standard deviations.

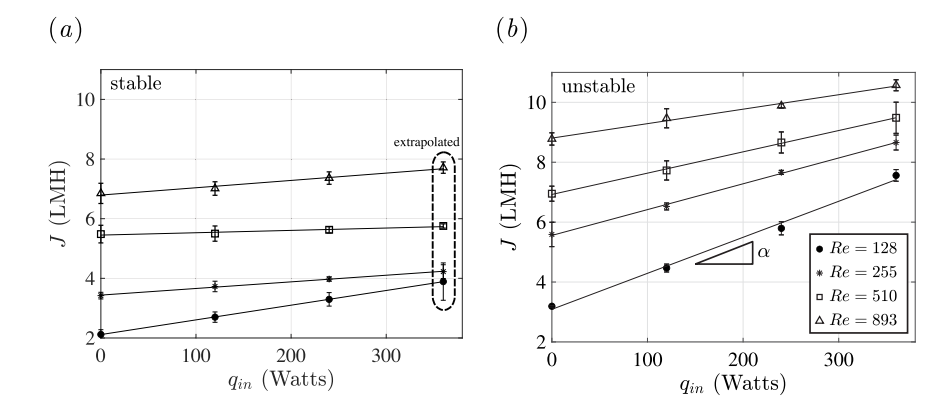


Fig. 7. Permeate flux J versus wall heat q_p when treating a feed solution of 70 g/L NaCl in the stable (panel a) and unstable (panel b) orientations. Symbols show the measured data with error bars. Solid lines how linear best fits. In panel (a), the flux at $q_p = 360$ W is extrapolated.

3. Results

Section 3.1 presents a parametric study that varies the wall heat between $0 \le q_p \le 360$ W, for the stable and unstable orientations, and the feed Reynolds numbers listed in Table 1. These experiments treat a feed with 70 g/l NaCl, with no feed spacer. Subsequently, Section 3.2 considers DI water as the feed, so that density variations only arise due to temperature variations. Finally, Section 3.3 considers the impact of a feed spacer.

3.1. Impact of orientation, wall heating, and feed Reynolds number

Fig. 7 shows the measured permeate flux J as a function of the wall heat q_p when treating a feed solution of 70 g/L NaCl with no feed spacer. Panels (a) and (b) show results for the stable and unstable orientations, respectively. Results are shown for the feed Reynolds numbers Re^f listed in the legend. The symbols show the measured data, while the solid lines show linear best fits. We are unable to perform experiments at $q_p=360$ W in the stable orientation, because the temperature of the acrylic plate exceeds 100 °C. The data circled in panel (a) is extrapolated linearly from the results at lower wall heating.

From Fig. 7, it is clear that the unstable orientation produces significantly more permeate than the stable orientation, even without wall heating ($q_p=0$). This suggests that buoyancy-driven convection occurs even in the absence of wall heating. For both orientations, J increases with q_p and Re^f . The data suggest that J increases linearly with q_p , and the rate of increase is much greater for the unstable orientation. We also observe that for the unstable orientation, the slopes of the linear fits (labeled α in Fig. 7b) decrease with increasing Re^f . This suggests that with increasing heat q_p , the permeate flux produced by $Re^f=128$ could surpass that produced by $Re^f=893$. Extrapolation predicts that this occurs when $q_p>794$ W. However, such a high value is likely impractical.

The impact of orientation, Re^f , and q_p are further quantified in Table 1, which lists the relative increase in flux $\Delta J = (J_{360} - J_0)/J_0$, where J_0 and J_{360} are the fluxes at $q_p = 0$ and 360 W, respectively. J_{360} is extrapolated for the stable case. Fig. 8 plots the variation of ΔJ with Re^f for the stable (solid line) and unstable (dashed line) orientations. For the unstable orientation, ΔJ decreases monotonically from 137% at $Re^f = 128$ to 20.4% at $Re^f = 893$. This likely occurs because the downstream feed flow has a stabilizing effect that delays the onset of convection. This effect is known for the related problem of mixed convection heat transfer in channel flows with a heated wall [28,29]. In that case, experiments show that increasing the Reynolds number pushes the onset of convection downstream from the inlet [28,29].

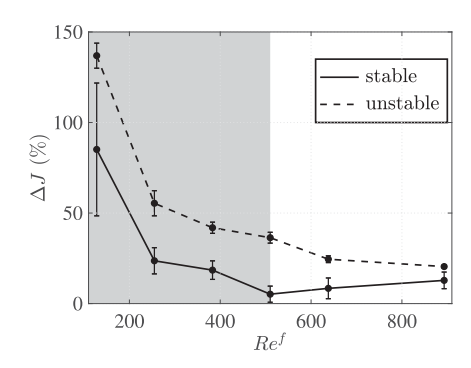


Fig. 8. Variation of ΔJ with Re_{in}^f for the stable (solid lines) and unstable (dashed lines) orientations. Symbols show the measured data with error bars.

This occurs because increasing the Reynolds number decreases the thermal boundary layer thickness and the temperature difference therein. Conversely, increasing the heat flux through the plate increases the boundary layer thickness and pushes onset upstream, closer to the inlet. Identical behavior was observed in our CFD simulations of buoyancy-driven convection in VMD [22], where increasing the Reynolds number was found to decrease the thicknesses of the thermal and solutal boundary layers growing on the plate and membrane. This pushed onset of convection downstream, and in some cases, outside the simulated length.

Though it is tempting to compare the current problem with Rayleigh-Bénard-Poiseuille (RBP) flow, the comparison is less straightforward, because RBP flow considers channel flow with a linear temperature profile. In contrast, the current problem has nonlinear temperature profiles in the thermal boundary layers. We nevertheless note here that increasing the Reynolds numbers can also delay convection in RBP flow; however, it depends on whether the convection takes the form of transverse or longitudinal roles [30–35]. The former are delayed by increasing the Reynolds number, while the latter are insensitive.

Fig. 8 shows that for the stable orientation, ΔJ initially decreases between $128 \leq Re_f \leq 510$ (shaded gray), after which ΔJ increases. This non-monotonic behavior could be explained as follows. In the absence of buoyancy-driven convection or other mixing, laminar thermal boundary layers grow along both the membrane and the heated plate, and the membrane is unaffected by wall heating until the two thermal boundary layers have grown sufficiently to interact. Increasing the feed Reynolds number decreases the boundary layer thicknesses, and

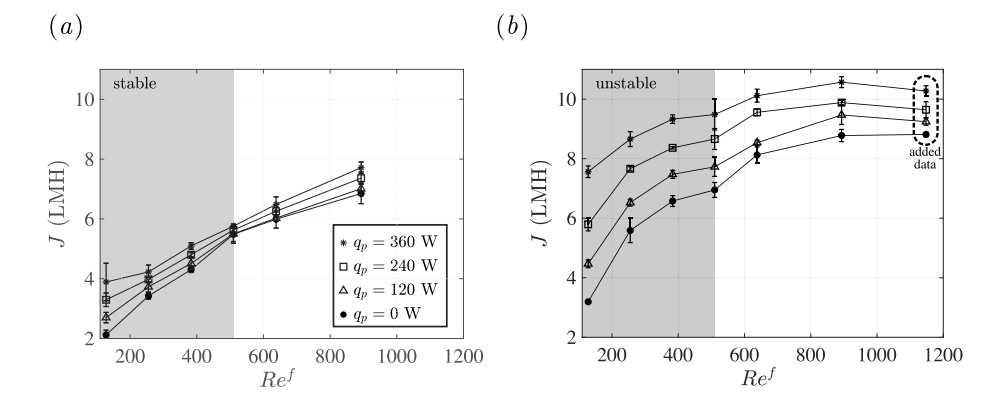


Fig. 9. J versus Re^f for the stable (panel a) and unstable (panel b) orientations. Results are shown for $q_p = 0$ (solid dots), 120 W (triangles), 240 W (squares), and 360 W (asterisks). Panel (b) includes data from an added run at $Re^f = 1148$. Symbols show the measured data with error bars.

increases the initial downstream distance over which the membrane is unaffected by q_p . The increase in ΔJ for $Re^f>510$ might be explained by a change in flow regime that brings heat to the membrane, such as the appearance of secondary vortical flows or a transition to turbulence. Experimental confirmation of that hypothesis is not possible, because the plate and membrane are optically opaque. We also note that the error bars for the stable case in Fig. 8 are larger than for the unstable case due to uncertainty introduced through the linear extrapolation of J_{360} .

Fig. 9 shows the variation of J with Re^f for the stable (panel a) and unstable (panel b) orientations. Results are shown for $q_p=0$, 120, 240, and 360 W (see legend). The region $Re^f \leq 510$ is shaded gray to aid our discussion. In the stable orientation, J tends to increase linearly with Re^f , but with a change in slope at $Re^f=510$. This slope change could be explained by our hypothesis that there is a change in flow regime around $Re^f=510$. It is tempting to suggest that a change in slope is also evident in panel (b) for the unstable orientation. However, the error bars at that Reynolds number suggest the change in slope could simply be due to outliers in our data.

In the unstable orientation, J varies nonlinearly with Re^f , and is far more sensitive to a_p . This is likely due to enhanced mixing from buoyancy-driven convection. When we consider the data up to $Re^f = 893$, J appears to plateau at high Reynolds numbers. This motivated us to run an additional set of experiments at $Re^f = 1148$, which is the maximum attainable in our system. The additional data points in panel (b) suggest that J begins to decrease when $Re^f > 893$. This likely occurs due to a suppression of buoyancy-driven convection at high feed Reynolds numbers, as discussed in Fig. 8.

Fig. 10(a) shows the percentage of wall heat contributing to distillate production (β^{evp}) in the stable (solid line) and unstable (dashed line) orientations. The data is computed when $q_p=240$ W, and is shown as a function of Re^f . As expected, a greater percentage of q_p contributes to evaporation in the unstable orientation. The percentage in the unstable orientation also decreases as Re^f increases, from 24.8% at $Re^f=128$ to 10.5% at $Re^f=893$. Fig. 10(b) shows the corresponding percentage of wall heat that exits the feed channel outlet (β^{out}). For the stable orientation, β^{out} increases with Re^f from 61.8% at $Re^f=128$ to 90.8% at $Re^f=893$. We conclude that in the stable orientation, most of the supplied wall heat is simply carried out of the feed channel. For the unstable orientation, β^{out} is much less, but still increases with Re^f from 27.5% at $Re^f=128$ to 77.7% at $Re^f=893$.

For the unstable orientation, β^{out} could be substantially reduced using a longer membrane to provide more time for plumes to advect heat to the membrane. Heat leaving the feed outlet could also be captured in a secondary heat recovery, or recycled by returning concentrate to

the feed inlet, as in a semi-batch process. Finally, transmembrane heat conduction could be minimized using VMD, though this comes with added complexity. Overall, however, it is worth stressing that heat lost to concentrate is perhaps the main disadvantage of wall heating in comparison to heating the membrane directly [6–15]. For comparison, prior work suggests that heated membranes in VMD lose as little as 16% of the supplied heat to the concentrate [15].

Table 1 lists the fractions β^{evp} , β^{out} , and β^{cnd} computed when $q_p = 240$ W. Note that the stable orientation has a negative β^{cnd} when $Re^f = 893$. This occurs because the estimated q_{cnd} at $q_p = 240$ W is slightly less than q_{cnd}^0 , generating a negative numerator in Eq. (3). The negative value is close to zero, and likely arises due to a combination of experimental uncertainty and the approximations made in our energy balance.

Prior MD literature often computes a thermal efficiency η , defined as the fraction of transmembrane heat transport occurring due to permeate production [36]. In a system with no transmembrane heat conduction, this efficiency is $\eta=1$. We similarly define the thermal efficiency η_{α} ,

$$\eta_q = \frac{\beta^{evp}}{\beta^{evp} + \beta^{cnd}} , \qquad (6)$$

which represents the fraction of wall heating transferred to the distillate channel due to permeate production (β^{evp}), to the total fraction of wall heating transferred to the distillate channel ($\beta^{evp} + \beta^{end}$).

Table 1 lists η_q when $q_p = 240$ W. For the unstable orientation, η_q varies between 41.5–55.1%, which is consistent with η values observed in conventional DCMD systems [36].

3.2. Role of concentration polarization

To help distinguish the compounding roles of temperature polarization, concentration polarization, and the heated plate, we run a set of experiments using DI water as the feed. In that case, there is no concentration polarization, and when $q_p=0$, density variations only arise due to temperature polarization at the membrane. When $q_p>0$, additional density variations occur over the surface of the heated plate. As in the previous section, there is no feed spacer over the active membrane area. For brevity, we consider only two feed flow rates, $U_{in}^f=1.64$ and 11.5 cm/s. These are the lower and upper limits of U_{in}^f considered in Table 1. For a feed of pure DI water, these flow rates produce $Re^f=142$ and 993, respectively. These values are slightly larger than the Re^f listed in Table 1, because DI water has a smaller kinematic viscosity than a feed of 70 g/l NaCl.

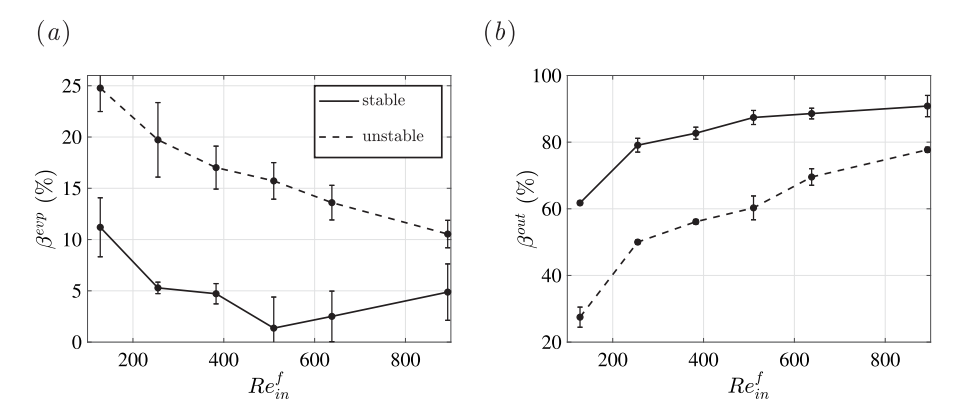


Fig. 10. Variation of β^{evp} (panel a) and β^{out} (panel b) as a function of Re^f for the stable (solid lines) and unstable (dashed lines) orientations when $q_p = 240$ W. Symbols show the measured data with error bars.

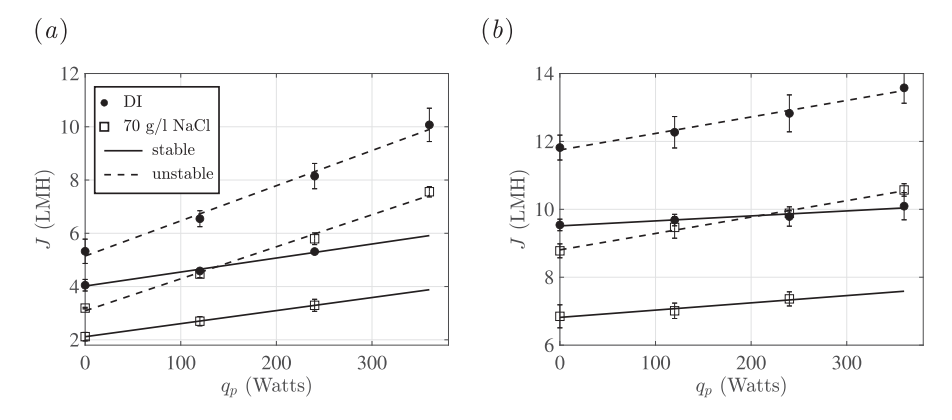


Fig. 11. Variation of J with q_p for a feed of DI water (solid dots) and a feed of 70 g/l NaCl (squares). Results are shown for the stable (solid lines) and unstable (dashed lines) orientations when $U_{in}^f = 1.64$ cm/s (panel a) and $U_{in}^f = 11.5$ cm/s (panel b). The lines show linear best fits. Absence of data at $q_p = 360$ W indicates the plate temperature exceeded 100 °C.

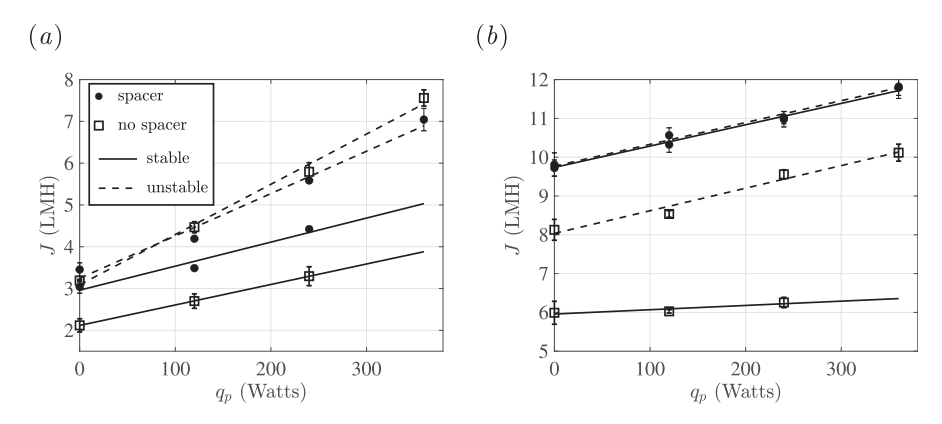


Fig. 12. Variation of J with q_p when treating a solution of 70 g/l NaCl with a feed spacer (solid dots) and without a feed spacer (square symbols). Results are shown for the stable (solid lines) and unstable (dashed lines) orientations when $Re^f = 128$ (panel a) and $Re^f = 638$ (panel b). The lines show linear best fits. Absence of data at $q_p = 360$ W indicates the plate temperature exceeded 100 °C.

Fig. 11 shows the variation of J with q_n for a feed of DI water (solid dots) and a feed of 70 g/l NaCl (square symbols). Results are shown in the stable (solid lines) and unstable (dashed lines) orientations. Panels (a) and (b) show results when $U_{in}^f = 1.64$ and 11.5 cm/s, respectively. In some cases, there are no data points at $q_n = 360$ W for the stable orientation, because the plate temperature exceeds 100 °C. We first note that when the feed is DI water, the unstable orientation always produces more permeate than the stable orientation, even when $q_p = 0$. This suggests that temperature polarization is the primary driver of any buoyancy-driven instability originating from the nearmembrane region. For both flowrates and orientations, the feed of DI water produces more permeate flux than the feed with NaCl. Overall, the feed composition has negligible impact on the slopes of the linear best fits. The addition of NaCl simply shifts the best fits downward. This result is perhaps counter-intuitive. On one hand, one might expect the permeate flux to decrease with the addition of NaCl, because NaCl decreases the feed partial vapor pressure. On the other hand, one might expect the presence of NaCl to promote buoyancy-driven convection, because concentration polarization increases the feed density near the membrane. Overall, Fig. 11 suggests that temperature polarization and wall-heating are the primary drivers of buoyancy-driven convection for the operating conditions considered here.

3.3. Impact of a feed spacer

To explore how a feed spacer affects buoyancy-driven convection, we run a final set of experiments in which we treat a feed solution of 70 g/l NaCl using a feed spacer over the full active membrane area. The feed spacer is identical to that in the distillate channel. The experiments consider $Re^f=128$ and 638. We do not consider $Re^f=893$, because the distillate chiller cannot maintain the desired distillate temperature with a feed spacer at that Reynolds number.

Fig. 12(a) shows the resulting variation of J with q_n when $Re^f =$ 128. Results are shown using a feed spacer (solid dots) and without a feed spacer (square symbols), both in the stable (solid lines) and unstable (dashed lines) orientations. Focusing on the results with a spacer, we see that the unstable orientation produces significantly more permeate flux. We conclude that for this low Reynolds number, the mixing generated by the spacer is not the dominant mechanism of heat transport, and buoyancy-driven convection remains important. If we focus on results in the stable orientation, we see that the addition of a feed spacer increases permeate production. This is expected, because buoyancy-driven convection does not occur in the stable orientation. In that case, the feed spacer generates mixing that helps transport q_n to the membrane. For the unstable orientation, we see that the permeate flux is comparable both with and without a feed spacer. That suggests that for this low Reynolds number, simple buoyancy-driven convection mixes the feed just as well as a spacer.

Fig. 12(b) shows the variation of J with q_p when $Re^f=638$. At this high Reynolds number, gravitational orientation has no impact on permeate production when using a feed spacer. The feed spacer also increases permeate production. This suggests that at higher Reynolds numbers, the spacer dominates fluid mixing, and does a better job of transporting heat from the plate to the membrane than buoyancy-driven convection without a spacer. Though we find that feed spacers improve heat transport at higher Reynolds numbers, further study is required to explore the impact of feed spacers on mineral scaling. Prior work shows that while feed spacers tend to increase permeate production, they can also counter-intuitively increase concentration polarization [17,37]. This occurs because feed spacers can reduce temperature polarization while simultaneously generating regions of preferential solute accumulation on the membrane.

4. Conclusions

For all feed Reynolds numbers (Re^f) and wall heat fluxes (q_p) considered, the unstable orientation produces considerably more permeate flux (J) than the stable orientation. Because the membrane and surface heater are opaque, we cannot observe the flow fields directly. We hypothesize that the impact of orientation occurs due to buoyancy-driven convection, because that mechanism is known in related heat transfer and hydrodynamic stability literature [28–33] and was independently observed in our CFD simulations of VMD [22].

For the unstable orientation, the permeate flux increases linearly with wall heating. The rate of flux increase with q_p also increases as the feed Reynolds number decreases. We hypothesize that this occurs because increasing the feed Reynolds number decreases the thermal boundary layer thicknesses. This effect is known for mixed convection heat transfer in channel flows [28,29], and was observed in our prior CFD simulations [22]. At $Re^f=893$, we observed a 20.7% increase in flux as q_p was raised to 360 W. In contrast, at $Re^f=128$ the flux increased more than 130%.

Our energy balance suggests that only a fraction of the wall heat q_p successfully contributes to evaporation at the membrane surface. For the unstable orientation, this fraction decreases from $\beta^{evp}=24.8\%$ at $Re^f=128$ to $\beta^{evp}=10.5\%$ at $Re^f=893$. At higher Reynolds numbers, most of the wall heat is carried out of the feed channel. We expect that β^{evp} can be increased, and β^{out} decreased by simply using a longer membrane to provide more time for plumes to advect heat to the membrane. The heat exiting the feed channel can also be captured through a secondary heat recovery step or by simply returning concentrate back to the feed inlet. This is left to future work.

To help distinguish the compounding roles of temperature and concentration polarization, we ran a series of experiments using DI water as feed. The results suggest that temperature polarization and wall-heating are the primary drivers of buoyancy-driven convection in DCMD. Finally, to investigate the impact of a feed spacer on convection and heat transport, we ran a series of experiments with a feed spacer over the active membrane area. These experiments showed that while buoyancy-driven convection remains influential at lower feed Reynolds numbers ($Re^f \sim 100$), the spacer dominates mixing at higher Re^f ($Re^f \sim 600$), such that there is no influence of gravitational orientation. Moreover, the feed spacer also increased the permeate flux from that observed without a feed spacer.

Our results raise numerous avenues for future work, of which we note 7 below. (1) To minimize any impact of membrane flapping or warping, we operated our DCMD system in co-current mode. We expect the permeate flux to improve further when operated in counter-current mode. (2) Buoyancy-driven convection can occur over vertical and inclined surfaces as well [28]. In a spiral wound system, a vertical orientation is worth investigating, because in a horizontal orientation, roughly half of the membrane surface area in a spiral wound module will be in a stable orientation. (3) To conserve membrane material, our heated cell had an active membrane length of 30 cm. We expect wall heating to become more effective over longer membranes that provide more time for heat to travel between the wall and membrane. (4) We expect the thermal efficiency η_p to improve in VMD, AGMD, or SGMD systems, for which conductive heat losses are much less. (5) Our work raises the question of whether wall heating is better implemented by operating a system at a lower Re^f without a feed spacer, or at higher Re^f with a feed spacer. Moreover, there is the option of texturing the heated wall with structures such as fins or dimples that support the membrane, as sketched in Fig. 13, so that no feed spacer is required. Fin-type structures, such as those in panels (a) and (b), could add a component of conductive heat transport towards the membrane, but would likely exacerbate concentration polarization at the contact lines between the fin and membrane. Alternatively, dimple-type structures, such as those in panel (c) could potentially be arranged to mitigate concentration polarization. These issues should be investigated using

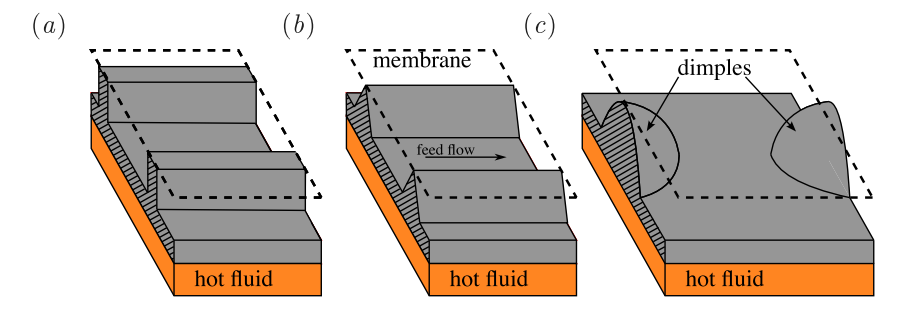


Fig. 13. Future work could consider fins (as in panels a and b) or other structures (as in panel c) that support the membrane while improving heat transport and/or mitigating concentration polarization.

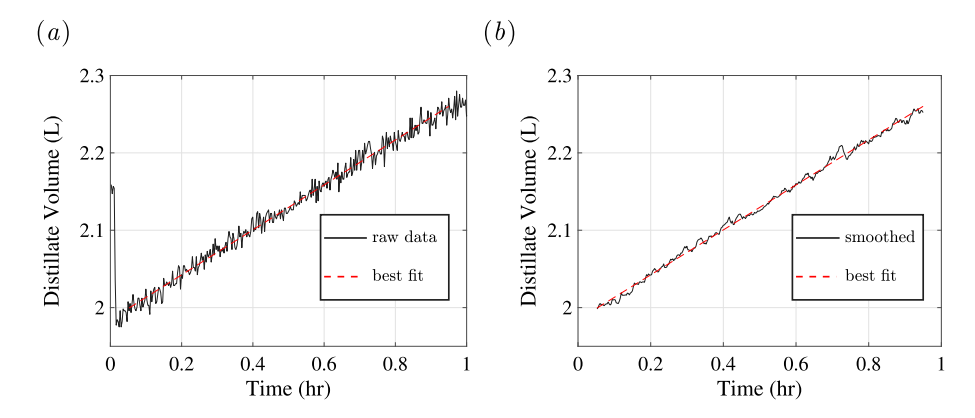


Fig. 14. (a) Comparison of raw data (solid line) and linear best fit (dashed red line) for the distillate tank volume as a function of time. (b) Comparison of smoothed data (solid black line) and linear best fit (red dashed line).

dedicated CFD, and explored experimentally using feed solutions with a sparingly soluble salt, such as $CaSO_4$, to explore their impact on mineral scaling. (6) Future work should also consider the feasibility of heating the plate using a secondary hot fluid, as sketched in Fig. 13. At the pilot-scale, that approach brings the significant challenge of pumping and distributing a secondary fluid through tightly packed membranes. (7) Buoyancy should be explored in studies of heated membranes, because those studies consider Reynolds numbers as low as $Re^f \sim 0.1$, where buoyancy could play a significant positive or negative role.

CRediT authorship contribution statement

Miles Mabry: Writing - original draft, Methodology, Investigation, Formal analysis, Data curation, Conceptualization. Federico Municchi: Validation, Investigation, Formal analysis, Conceptualization. Yiming Liu: Investigation, Data curation. Jingbo Wang: Investigation, Data curation. Tzahi Y. Cath: Writing - review & editing, Writing original draft, Validation, Supervision, Resources, Project administration, Methodology, Investigation, Funding acquisition, Formal analysis, Data curation, Conceptualization. Craig S. Turchi: Investigation, Formal analysis, Conceptualization. Michael B. Heeley: Investigation, Formal analysis, Conceptualization. Eric M.V. Hoek: Investigation, Formal analysis, Conceptualization. David Jassby: Writing - review & editing, Validation, Supervision, Resources, Project administration, Methodology, Investigation, Funding acquisition, Formal analysis, Data curation, Conceptualization. Denis Martinand: Writing - review & editing, Formal analysis, Conceptualization. Nils Tilton: Writing review & editing, Writing - original draft, Visualization, Validation, Supervision, Software, Resources, Project administration, Methodology, Investigation, Funding acquisition, Formal analysis, Data curation.

Declaration of competing interest

The authors declare that they have no known competing financial interests or personal relationships that could have appeared to influence the work reported in this paper.

Data availability

Data will be made available on request.

Acknowledgments

This work was generously supported by the U.S. Department of Energy (Award No. DE-EE0008391), the National Science Foundation (grant numbers 1752531 and 2306329), the Embassy of France Thomas Jefferson Fund, and the Colorado Office of Economic Development and International Trade. We thank Mike Veres, Tani Cath, Alex Schwiebert and Dr. Johan Vanneste at the Colorado School of Mines for technical lab support. We also thank Drs. Steven DeCaluwe (Colorado School of Mines) and John Farnsworth (University of Colorado, Boulder) for helpful conversations.

Appendix A. Permeate flux measurement

The solid black line in Fig. 14(a) shows the measured volume in the distillate tank as a function of time. To compute J, noise from the initial filling of the tank is cropped, and the signal is smoothed using Matlab's "movmean" function. This produces the solid black line in panel (b). We then use Matlab's "polyfit" command to determine the best linear fit to the smoothed data, producing the red dashed line in panels (a) and (b).

Appendix B. Thermophysical properties

We express the variation of μ , ρ and c_p with temperature and concentration using bivariate polynomials of the form

$$f(T,c) = \sum_{n=0}^{3} \sum_{m=0}^{4} a_{nm} T^{n} c^{m}.$$
 (7)

 Table 2

 Polynomial coefficients for the thermophysical properties.

	μ (Pa s)	$c_p \ ({\rm J} \ {\rm kg}^{-1} \ {\rm K}^{-1})$	ρ (kg/m ³)
a_{00}	0.04916	4375	1112
a_{10}	-0.0003892	-1.91	-0.2853
a_{01}	9.997e-05	-4.645	0.881
a_{11}	-8.7e-07	0.003891	-0.0003063
a_{20}	1.042e-06	-0.0001738	-0.0006925
a_{02}	1.022e-07	0.002118	-0.0001679
a_{30}	-9.385e-10	0	0
a_{21}	2.564e-09	0	0
a_{12}	-8.7e-07	0	0
a_{03}	1.488e-11	0	0
a_{31}	-2.535e-12	0	0
a_{22}	8.131e-13	0	0
a ₁₃	-5.766e-10	0	0
a_{04}	-1.598e-15	0	0

We determine the coefficients a_{nm} by fitting (using MATLAB's "polyfit" command) to data from thermodynamic software (OLI [38]). The polynomial coefficients are given in Table 2. To reduce the polynomial order of some correlations, coefficients that do not affect the accuracy significantly are set to zero.

References

- R.W. Schofield, A.G. Fane, C.J.D. Fell, Heat and mass transfer in membrane distillation, J. Membr. Sci. 33 (1987) 299–313.
- [2] K.W. Lawson, D.R. Lloyd, Review of membrane distillation, J. Membr. Sci. 124 (1997) 1–25.
- [3] M. Khayet, Membranes and theoretical modeling of membrane distillation: A review, Adv. Colloid Interface Sci. 164 (2011) 56–88.
- [4] X. Chen, N.Y. Yip, Unlocking high-salinity desalination with cascading osmotically mediated reverse osmosis: Energy and operating pressure analysis, Environ. Sci. Technol. 52 (2018) 2242–2250.
- [5] K.L. Hickenbottom, T.Y. Cath, Sustainable operation of membrane distillation for enhancement of mineral recovery from hypersaline solutions, J. Membr. Sci. 454 (2014) 426–435.
- [6] A.V. Dudchenko, C. Chen, A. Cardenas, J. Rolf, D. Jassby, Frequency-dependent stability of CNT joule heaters in ionizable media and desalination processes, Nat. Nanotechnol. 12 (2017) 557–564.
- [7] K. Li, Y. Zhang, Z. Wang, L. Liu, H. Liu, J. Wang, Electrothermally driven membrane distillation for low-energy consumption and wetting mitigation, Environ. Sci. Technol. 53 (2019) 13506–13513.
- [8] J. Huang, Y. He, Z. Shen, Joule heating membrane distillation enhancement with multi-level thermal concentration and heat recovery, Energy Convers. Manage. 238 (2021) 114111.
- [9] M. Mustakeem, A. Qamar, A. Alpatova, N. Ghaffour, Dead-end membrane distillation with localized interfacial heating for sustainable and energy-efficient desalination, Water Res. 189 (2021) 116584.
- [10] A. Anvari, K.M. Kekre, A. Azimi Yancheshme, Y. Yao, A. Ronen, Membrane distillation of high salinity water by induction heated thermally conducting membranes, J. Membr. Sci. 589 (2019) 117253.
- [11] P.D. Dongare, A. Alabastri, S. Pedersen, K.R. Zodrow, N.J. Hogan, O. Neumann, J. Wu, T. Wang, A. Deshmukh, M. Elimelech, Q. Li, P. Nordlander, N.J. Halas, Nanophotonics-enabled solar membrane distillation for off-grid water purification, Proc. Natl. Acad. Sci. USA 114 (2017) 6936–6941.
- [12] Y.-S. Jun, X. Wu, D. Ghim, Q. Jiang, S. Cao, S. Singamaneni, Photothermal membrane water treatment for two worlds, Acc. Chem. Res. 52 (5) (2019) 1215–1225
- [13] J. Wang, Y. Liu, U. Rao, M. Dudley, N.D. Ebrahimi, J. Lou, F. Han, E.M. Hoek, N. Tilton, T.Y. Cath, C.S. Turchi, M.B. Heeley, Y.S. Ju, D. Jassby, Conducting thermal energy to the membrane/water interface for the enhanced desalination of hypersaline brines using membrane distillation, J. Membr. Sci. 626 (2021) 119188.
- [14] Y. Liu, J. Wang, B. Jung, U. Rao, E. Sedighi, E.M. Hoek, N. Tilton, T.Y. Cath, C.S. Turchi, M.B. Heeley, Y.S. Ju, D. Jassby, Desalinating a real hyper-saline pre-treated produced water via direct-heat vacuum membrane distillation, Water Res. 218 (2022) 118503.

- [15] J. Lou, M. Dudley, J. Wang, Y. Liu, T.Y. Cath, C.S. Turchi, M.B. Heeley, E.M. Hoek, D. Jassby, N. Tilton, Numerical simulations of membrane distillation systems with actively heated membranes, J. Membr. Sci. 668 (2023) 121206.
- [16] J. Lou, J. Vanneste, S.C. DeCaluwe, T.Y. Cath, N. Tilton, Computational fluid dynamics simulations of polarization phenomena in direct contact membrane distillation, J. Membr. Sci. 591 (2019).
- [17] J. Lou, J. Johnston, T.Y. Cath, D. Martinand, N. Tilton, Computational fluid dynamics simulations of unsteady mixing in spacer-filled direct contact membrane distillation channels. J. Membr. Sci. 622 (2021) 118931.
- [18] M. Gryta, M. Tomaszewska, A. Morawski, Membrane distillation with laminar flow, Sep. Purif. Technol. 11 (2) (1997) 93–101.
- [19] S. Bouguecha, R. Chouikh, M. Dhahbi, Numerical study of the coupled heat and mass transfer in membrane distillation, Desalination 152 (1) (2003) 245–252, http://dx.doi.org/10.1016/S0011-9164(02)01070-6, URL https://www.sciencedirect.com/science/article/pii/S0011916402010706.
- [20] Y.Z. Tan, L. Han, W.H. Chow, A.G. Fane, J.W. Chew, Influence of module orientation and geometry in the membrane distillation of oily seawater, Desalination 423 (2017) 111–123.
- [21] J. Caspar, G. Xue, J. Asiri, A. Oztekin, The Effect of Buoyancy-Driven Convection in Vacuum Membrane Distillation Module, in: ASME International Mechanical Engineering Congress and Exposition, Volume 8: Fluids Engineering; Heat Transfer and Thermal Engineering, 2022, V008T10A031.
- [22] F. Municchi, Y. Liu, J. Wang, T.Y. Cath, C.S. Turchi, M.B. Heeley, E.M. Hoek, D. Jassby, N. Tilton, A numerical method for simulating variable density flows in membrane desalination systems, Comput. & Fluids Submitted (2023).
- [23] J.A. Bush, J. Vanneste, T.Y. Cath, Membrane distillation for concentration of hypersaline brines from the great salt lake: Effects of scaling and fouling on performance, efficiency, and salt rejection, Sep. Purif. Technol. 170 (2016) 78-91
- [24] J. Vanneste, J.A. Bush, K.L. Hickenbottom, C.A. Marks, D. Jassby, C.S. Turchi, T.Y. Cath, Novel thermal efficiency-based model for determination of thermal conductivity of membrane distillation membranes, J. Membr. Sci. 548 (2018) 298–308.
- [25] R. Knikker, A comparative study of high-order variable-property segregated algorithms for unsteady low mach number flows, Internat. J. Numer. Methods Fluids 66 (4) (2011) 403–427.
- [26] M. Mabry, Instigating Buoyancy Driven Convection to Improve Membrane Distillation Performance (Master's thesis), Colorado School of Mines, 2023.
- [27] J. Vanneste, J.A. Bush, K.L. Hickenbottom, C.A. Marks, D. Jassby, C.S. Turchid, T.Y. Cath, Novel thermal efficiency-based model for determination of thermal conductivity of membrane distillation membranes, J. Membr. Sci. 548 (2018) 298–308.
- [28] J.R. Maughan, F.P. Incropera, Experiments on mixed convection heat transfer for airflow in a horizontal and inclined channel, Int. J. Heat Mass Transfer 30 (1987) 1307–1318.
- [29] J.R. Maughan, F.P. Incropera, Regions of heat transfer enhancement for laminar mixed convection in a parallel plate channel, Int. J. Heat Mass Transfer 33 (1990) 555–570.
- [30] R. Kelly, in: J.W. Hutchinson, T.Y. Wu (Eds.), The Onset and Development of Thermal Convection in Fully Developed Shear Flows, in: Advances in Applied Mechanics, vol. 31, Elsevier, 1994, pp. 35–112.
- [31] K. Fujimura, R.E. Kelly, Interaction between longitudinal convection rolls and transverse waves in unstably stratified plane poiseuille flow, Phys. Fluids 7 (1) (1995) 68–79.
- [32] P. Carrière, P.A. Monkewitz, Convective versus absolute instability in mixed Rayleigh–Bénard–Poiseuille convection, J. Fluid Mech. 384 (1999) 243–262.
- [33] X. Nicolas, Revue bibliographique sur les écoulements de Poiseuille-Rayleigh-Bénard: écoulements de convection mixte en conduites rectangulaires horizontales chauffées par le bas, Int. J. Therm. Sci. 41 (10) (2002) 961–1016.
- [34] P. Carrière, P.A. Monkewitz, D. Martinand, Envelope equations for the Rayleigh-Bénard-Poiseuille system. Part 1. Spatially homogeneous case, J. Fluid Mech. 502 (2004) 153–174.
- [35] D. Martinand, P. Carrière, P.A. Monkewitz, Three-dimensional global instability modes associated with a localized hot spot in Rayleigh–Bénard–Poiseuille convection, J. Fluid Mech. 551 (2006) 275–301.
- [36] J. Swaminathan, H.W. Chung, D.M. Warsinger, J.H. Lienhard V, Membrane distillation model based on heat exchanger theory and configuration comparison, Appl. Energy 184 (2016) 491–505.
- [37] J. Johnston, S.M. Dischinger, M. Nassr, J.Y. Lee, P. Bigdelou, B.D. Freeman, K.L. Gleason, D. Martinand, D.J. Miller, S. Molins, N. Spycher, W.T. Stringfellow, N. Tilton, A reduced-order model of concentration polarization in reverse osmosis systems with feed spacers, J. Membr. Sci. 675 (2023) 121508.
- [38] OLI Systems, Inc. URL https://www.olisystems.com/.